Journal of the Mechanics and Physics of Solids 61 (2013) 370–384

Contents lists available at SciVerse ScienceDirect

Journal of the Mechanics and Physics of Solids

journal homepage: www.elsevier.com/locate/jmps

Grain boundary modeling using an elasto-plastic theory of dislocation and disclination fields

V. Taupin [a,*], L. Capolungo [b], C. Fressengeas [a], A. Das [a], M. Upadhyay [b]

[a] Laboratoire d'Etude des Microstructures et de Mécanique des Matériaux, Université de Lorraine/CNRS, Ile du Saulcy, 57045 Metz Cedex, France
[b] G.W. Woodruff School of Mechanical Engineering, Georgia Institute of Technology/CNRS, 57070 Metz Cedex, France

ARTICLE INFO

Article history:
Received 27 February 2012
Received in revised form
26 July 2012
Accepted 3 October 2012
Available online 23 October 2012

Keywords:
Disclinations
Dislocations
Grain boundary
Strain gradient

ABSTRACT

Using a recent elasto-plastic theory of dislocation and disclination fields, a continuous representation of grain boundaries is introduced. Periodic arrays of wedge disclination dipoles, including those defined in the Disclination Structural Unit Model, are set-up as initial configurations in a dynamic model for symmetric tilt boundaries. These configurations are found to be unstable when the transport of disclinations is allowed. Driven by their self couple-stress field, the motion of disclinations leads to relaxation of the initial elastic curvature and stress fields and to nucleation and transport of relaxation dislocations, until an equilibrium configuration of lower energy is reached. Most of the residual elastic energy of grain boundaries is localized in a non-singular nanometric layer. This energy arises from alternative dilatation and contraction of the lattice around disclinations, and from lattice curvature and shear between disclination dipoles. By virtue of its continuous and dynamic character, the present theory allows modeling absolute misorientations and leads to energy density levels comparable to molecular statics findings.

1. Introduction

In the terminology of the differential geometry of continua as well as in the language of engineering, grain boundaries (GBs) in crystalline media are rotational defects resulting in discontinuities of the elastic/plastic strain and/or curvature fields along interfaces. Modeling efforts for the description of GBs include atomistic simulations (Sutton and Vitek, 1983; Cahn et al., 2006), dislocation/disclination-based models (Frank, 1950; Bilby, 1955; Li, 1972; Shih and Li, 1975; Gertsman et al., 1989; Cahn et al., 2006) and mechanical approaches (Wei and Anand, 2004; Warner et al., 2006; Gurtin and Anand, 2008; Wei et al., 2009; Zbib et al., 2011). From the atomistic standpoint, the continuum metrics needed for estimating the strain and curvature tensor fields is still to be built from the positions of the atoms in the interface region, and therefore a description of rotational incompatibility at GBs in continuum terminology is not derived yet. Nevertheless, such a framework has a strong potential at accurately rendering both the GB geometrical structure and excess free energy at sub-lattice length scale, as the success of the Peierls model in elucidating basic dislocation physics suggests. Thus, motivation exists for GB studies using the concepts of crystal defect fields (dislocations and disclinations). In early dislocation-based GB models, surface-dislocation densities were considered as the source of disorientation between grains, *i.e.*, an arbitrary

* Corresponding author.
E-mail address: vincent.taupin@univ-lorraine.fr (V. Taupin).

0022-5096/$ - see front matter © 2012 Elsevier Ltd. All rights reserved.
http://dx.doi.org/10.1016/j.jmps.2012.10.001

GB disorientation could be accommodated by an appropriate distribution of surface-dislocations (Frank, 1950; Bilby, 1955). These models are efficient at predicting geometrical properties of GBs, such as the coupling factor relating the normal tilt boundary motion to an imposed shear displacement (Cahn et al., 2006). However, surface-dislocations-based models are necessarily limited to small misorientation angles. Indeed, as implied by Frank's equation (Li, 1972) the distance between surface-dislocations decreases with an increase in misorientation angle to the point where dislocation core overlapping occurs. In addition, surface-dislocations are singularly supported by an infinitely thin interface, a premise at odds with the atomistic rendering of GBs, which features elementary structures spreading over a finite-width layer, perhaps as thin as a nanometer, but definitely not vanishingly thin (Sutton and Vitek, 1983).

As an alternative to the dislocation-based approach, discrete disclination walls were introduced to represent GBs in the Disclination Structural Unit Model (DSUM) (Li, 1972; Shih and Li, 1975; Gertsman et al., 1989). As discussed by Li (1972), being themselves rotational defects, disclinations seem more appropriate than dislocations for GB modeling. In the DSUM, the strength, *i.e.*, the Frank vector modulus, and spatial distribution of the discrete disclination dipoles are defined geometrically according to atomistic structural unit configurations such as to reproduce the GB misorientation (Gertsman et al., 1989). The elastic excess energy of the boundary is estimated from closed-form solutions for discrete disclination dipoles (Huang and Mura, 1970; deWit, 1973). However, practical use of the DSUM remains limited. First, the DSUM only describes relative misorientations with respect to reference boundaries—corresponding to cusps in the GB energy *vs.* misorientation plot, and it needs arbitrary extra-terms to retrieve the GB energy obtained from atomistic simulations. Second, the elasto-plastic response of GBs to loading has so far not been envisioned. Indeed, plasticity mediated by disclinations is ignored, and therefore, the possible relaxation of the disclination dipole walls in their self stress and couple stress fields is overlooked. Finally, it is to be noted here that some materials, such as Cu, can exhibit significant departure from the DSUM (Spearot, 2005).

The incompatibility arising at GBs was also treated by continuum mechanics models. For instance in finite element-based modeling of polycrystals, a discontinuity of displacement arising at GBs can be accounted for using cohesive-interface models, which allows modeling slip and crack at grain boundaries in nanocrystalline materials (see *e.g.* Wei and Anand, 2004; Gurtin and Anand, 2008; Wei et al., 2009). Another elaborate description of the elasto-plastic response of GBs, not necessarily accounting for incompatibilities, uses interfacial elements with phenomenological prescriptions (Warner et al., 2006; Zbib et al., 2011). Similar approach has also been adopted in discrete dislocation dynamics simulations of multilayered systems (Zbib et al., 2011). For example, a constant frictional force is applied to dislocations crossing a coherent finite interface (Zbib et al., 2011). However, while existing models can reproduce some of the features of GBs, usually at least the misorientation, these models cannot account for plastic deformation mechanisms dominated by what is usually referred to as core contributions. The absorption or the emission of a glide dislocation by a GB is an example of such a mechanism.

The aim of the present paper is to extend the static and discrete DSUM into a continuous and dynamic description of GBs using a recent elasto-plastic theory of dislocation and disclination fields (Fressengeas et al., 2011, 2012). In the latter, a continuous distribution of the elastic energy in the GB area is obtained, and plasticity mechanisms through coupled transport of dislocation and disclination densities are described. Further, the account of the rotational incompatibility of the lattice provides for a stabilization of the "core" structure of dislocations. As a result, contributions to GB energy arising from dislocation-GB interactions can be accounted for. The theory will be applied to the simulation of $\langle 001 \rangle$ tilt boundaries in copper at low temperatures, for which a rich literature is existing. In a way similar to earlier static calculations (Upadhyay et al., 2011), initial dipole walls built from continuous disclination densities, will be set up according to the DSUM rules. In contrast to the DSUM however, initial wall configurations allowing to retrieve absolute misorientations will also be described. Moreover, initially confined to narrow patches, much less than a nanometer square, so that they can be compared with discrete disclination dipoles, the continuous disclination dipoles will be allowed to relax in their self stress and couple-stress fields, until self-organized structures of lower energy emerge. Specific objectives of our simulations include evidencing the benefits offered by a continuous rendition of translational and rotational lattice incompatibility, possibly below inter-atomic spacing, as well as providing for a realistic geometric and energetic description of GBs at the scale of the experimentally observed crystalline structural units. The consistency of the relaxed grain boundary patterns with atomistic structures resulting from molecular statics simulations will be checked, particularly in terms of their elastic energies. However, GBs with kinks or ledges or phase boundaries are beyond the scope of the present investigation, although they can be treated using discrete disclination dipoles (see for example the review Romanov and Kolesnikova, 2009), because such features involve discontinuities of the elastic/plastic distortion. The characterization of these patterns in a continuous framework requires defining crystal defects of higher order than the dislocations and disclinations inherent to the Volterra construction. Such a theory was proposed in Acharya and Fressengeas (2012), where the concept of generalized disclinations was introduced.

The paper is organized as follows. In Section 2, notations are settled. In Section 3, the elasto-plastic theory of dislocation and disclination fields is briefly recalled, with special reference to the elasto-static theory developed by DeWit (1970). Not detailed in the earlier paper (Fressengeas et al., 2011), the role of the skew-symmetric stresses in the balance of momentum and moment of momentum is emphasized. In Section 4, a plane edge-wedge model is set up for tilt boundaries. Section 5 is devoted to the implementation of initial conditions inspired from the DSUM to build initial tilt boundaries. Relaxation of these initial structures is analyzed in Section 6, in comparison with molecular statics data. Conclusions follow.

2. Notations

A bold symbol denotes a tensor. When there may be ambiguity, an arrow is superposed to represent a vector: $\overrightarrow{\mathbf{V}}$. The symmetric part of tensor $\mathbf{A}$ is denoted $\mathbf{A}^{sym}$. Its skew-symmetric part is $\mathbf{A}^{skew}$. The tensor $\mathbf{A}\cdot\mathbf{B}$, with rectangular Cartesian components $A_{ik}B_{kj}$, results from the dot product of tensors $\mathbf{A}$ and $\mathbf{B}$, and $\mathbf{A}\otimes\mathbf{B}$ is their tensorial product, with components $A_{ij}B_{kl}$. A represents the trace inner product of the two second order tensors $\mathbf{A}:\mathbf{B}=A_{ij}B_{ij}$, in rectangular Cartesian components, or the product of a higher order tensor with a second order tensor, *e.g.* $\mathbf{A}:\mathbf{B}=A_{ijkl}B_{kl}$. The cross product of a second-order tensor $\mathbf{A}$ and a vector $\mathbf{V}$, the **div** and **curl** operations for second-order tensors are defined row by row, in analogy with the vectorial case. For any base vector $\mathbf{e}_i$ of the reference frame

$$(\mathbf{A}\times\mathbf{V})^t\cdot\mathbf{e}_i=(\mathbf{A}^t\cdot\mathbf{e}_i)\times\mathbf{V} \tag{1}$$

$$(\mathbf{div}\,\mathbf{A})^t\cdot\mathbf{e}_i=\mathbf{div}(\mathbf{A}^t\cdot\mathbf{e}_i) \tag{2}$$

$$(\mathbf{curl}\,\mathbf{A})^t\cdot\mathbf{e}_i=\mathbf{curl}(\mathbf{A}^t\cdot\mathbf{e}_i) \tag{3}$$

In rectangular Cartesian components

$$(\mathbf{A}\times\mathbf{V})_{ij}=e_{jkl}A_{ik}V_l \tag{4}$$

$$(\mathbf{div}\,\mathbf{A})_i=A_{ij,j} \tag{5}$$

$$(\mathbf{curl}\,\mathbf{A})_{ij}=e_{jkl}A_{il,k} \tag{6}$$

where e_{jkl} is a component of the third-order alternating Levi-Civita tensor $\mathbf{X}$. A vector $\overrightarrow{\mathbf{A}}$ is associated with tensor $\mathbf{A}$ using its trace inner product with tensor $\mathbf{X}$

$$(\overrightarrow{\mathbf{A}})_k=-\frac{1}{2}(\mathbf{A}:\mathbf{X})_k=-\frac{1}{2}e_{ijk}A_{ij} \tag{7}$$

In the component representation, the spatial derivative with respect to a Cartesian coordinate is indicated by a comma followed by the component index. A superposed dot represents a material time derivative.

3. Review of the elasto-plastic theory of dislocation and disclination fields

In the present framework, it is assumed that the displacement vector $\mathbf{u}$ can be defined continuously at any point of a simply connected body undergoing elasto-plastic deformation. Hence, it is required that the displacement field represents a consistent shape change, possibly defined between atoms, below interatomic distance. Therefore, the total distortion tensor is defined as the gradient of the displacement $\mathbf{U}=\mathbf{grad}\,\mathbf{u}$. As such, it is curl-free

$$\mathbf{curl}\,\mathbf{U}=0 \tag{8}$$

This equation is a necessary condition for the integrability of the displacement $\mathbf{u}$.

Conversely, this equation is sufficient to assure the existence of a single-valued continuous solution $\mathbf{u}$ to the equation $\mathbf{U}=\mathbf{grad}\,\mathbf{u}$, up to a constant translation. Eq. (8) is referred to as the compatibility condition for the distortion $\mathbf{U}$. Defining the strain tensor $\boldsymbol{\epsilon}$ as the symmetric part of the distortion $\mathbf{U}$, the rotation tensor $\boldsymbol{\omega}$ as its skew-symmetric part and the associated rotation vector $\overrightarrow{\boldsymbol{\omega}}$ as

$$\overrightarrow{\boldsymbol{\omega}}=-\frac{1}{2}\boldsymbol{\omega}:\mathbf{X}=\frac{1}{2}\mathbf{curl}\,\mathbf{u} \tag{9}$$

Eq. (8) becomes

$$\mathbf{curl}\,\boldsymbol{\epsilon}+\mathrm{div}(\overrightarrow{\boldsymbol{\omega}})\mathbf{I}-\mathbf{grad}^t\,\overrightarrow{\boldsymbol{\omega}}=0 \tag{10}$$

where $\mathbf{I}$ is the identity tensor. Transposing, then taking the **curl** of Eq. (10) leads to

$$\mathbf{curl}\,\mathbf{curl}^t\,\boldsymbol{\epsilon}=0 \tag{11}$$

This relation is the classical Saint-Venant compatibility condition for the strain $\boldsymbol{\epsilon}$. It is a necessary condition for the integrability of the displacement $\mathbf{u}$. The trace of Eq. (10) similarly yields a compatibility condition for the rotation vector in the form

$$\mathrm{div}(\overrightarrow{\boldsymbol{\omega}})=0 \tag{12}$$

At this point, we define the elastic, $\boldsymbol{\kappa}_e$, plastic, $\boldsymbol{\kappa}_p$, and total, $\boldsymbol{\kappa}$, curvature tensors as

$$\boldsymbol{\kappa}_e=\mathbf{grad}\,\overrightarrow{\boldsymbol{\omega}_e} \tag{13}$$

$$\boldsymbol{\kappa}_p=\mathbf{grad}\,\overrightarrow{\boldsymbol{\omega}_p} \tag{14}$$

$$\boldsymbol{\kappa}=\mathbf{grad}\,\overrightarrow{\boldsymbol{\omega}}=\boldsymbol{\kappa}_e+\boldsymbol{\kappa}_p \tag{15}$$

In the above, the elastic and plastic curvatures ($\boldsymbol{\kappa}_e$,$\boldsymbol{\kappa}_p$) are curl-free and integrable quantities. In the present theory however, ($\boldsymbol{\kappa}_e$,$\boldsymbol{\kappa}_p$) are not supposed to be curl-free anymore, *i.e.*, the possibility of a rotational incompatibility is acknowledged. Then the rotation vectors ($\overrightarrow{\omega_e}$,$\overrightarrow{\omega_p}$) do not exist, and a non-zero tensor $\boldsymbol{\theta}$ such that

$$\boldsymbol{\theta} = -\mathbf{curl}\,\boldsymbol{\kappa}_p = \mathbf{curl}\,\boldsymbol{\kappa}_e \tag{16}$$

can be defined. $\boldsymbol{\theta}$ is the disclination density tensor, and Eq. (16) is part of the theory of crystal defects. On the one hand, Eq. (16) means that an incompatible plastic curvature, $\boldsymbol{\kappa}_p^{\perp}$, is associated with the presence of the disclination density $\boldsymbol{\theta}$ and, on the other hand, that the incompatible elastic curvature, $\boldsymbol{\kappa}_e^{\perp}$ is needed to ensure the continuity of matter in the presence of this density. To ensure that the incompatible parts ($\boldsymbol{\kappa}_e^{\perp}$,$\boldsymbol{\kappa}_p^{\perp}$) vanish identically throughout the body when $\boldsymbol{\theta}=0$, Eq. (16) must be replaced with

$$\boldsymbol{\theta} = -\mathbf{curl}\,\boldsymbol{\kappa}_p^{\perp} = \mathbf{curl}\,\boldsymbol{\kappa}_e^{\perp} \tag{17}$$

augmented with the side conditions $\mathbf{div}\,\boldsymbol{\kappa}_e^{\perp} = \mathbf{div}\,\boldsymbol{\kappa}_p^{\perp} = 0$ and $\boldsymbol{\kappa}_{\mathbf{e}}^{\perp}\cdot\mathbf{n} = \boldsymbol{\kappa}_{\mathbf{p}}^{\perp}\cdot\mathbf{n} = \mathbf{0}$ on the boundary with unit normal $\mathbf{n}$. These conditions ensure uniqueness of the solution. The disclination density defined in Eq. (17) is an aerial and tensorial rendition of the rotational incompatibility. The associated point-wise measure of incompatibility is the Frank vector, *i.e.*, the rotational closure defect of a circuit C, obtained by integrating the incompatible elastic curvatures along the circuit

$$\boldsymbol{\Omega} = \int_C \boldsymbol{\kappa}_e^{\perp}\cdot\mathbf{dr} \tag{18}$$

This rotation discontinuity is related to the disclination density by applying Stokes theorem to the surface S of normal $\mathbf{n}$ delimited by the circuit C.

$$\boldsymbol{\Omega} = \int_S \boldsymbol{\theta}\cdot\mathbf{n}\,dS \tag{19}$$

The continuity condition for disclinations

$$\mathbf{div}\,\boldsymbol{\theta} = 0 \tag{20}$$

follows directly from Eqs. (16) and (17). Since the rotation vectors ($\overrightarrow{\omega_e}$,$\overrightarrow{\omega_p}$) do not exist in the present theory, the corresponding elastic and plastic distortion tensors $\mathbf{U}_e$ and $\mathbf{U}_p$ are also undefined. Substituting the elastic and plastic curvatures ($\boldsymbol{\kappa}_e$,$\boldsymbol{\kappa}_p$), which now include an incompatible part, for ($\mathbf{grad}\,\overrightarrow{\omega_e}$, $\mathbf{grad}\,\overrightarrow{\omega_p}$) and using the above curl-trace procedure, allows splitting Eq. (10) into elastic and plastic components

$$\mathbf{curl}\,\boldsymbol{\epsilon}_e = +\boldsymbol{\alpha}+\boldsymbol{\kappa}_e^t-\mathrm{tr}(\boldsymbol{\kappa}_e)\mathbf{I} \tag{21}$$

$$\mathbf{curl}\,\boldsymbol{\epsilon}_p = -\boldsymbol{\alpha}+\boldsymbol{\kappa}_p^t-\mathrm{tr}(\boldsymbol{\kappa}_p)\mathbf{I} \tag{22}$$

Eq. (22) defines the incompatible plastic strain associated with the Nye's dislocation density tensor $\boldsymbol{\alpha}$ in the concurrent presence of plastic curvature, while Eq. (21) specifies the incompatible elastic strain needed to ensure the continuity of matter in the presence of dislocations and disclinations. Eqs. (21) and (22) are modified forms of the incompatibility equations $\mathbf{curl}\,\mathbf{U_e} = -\mathbf{curl}\,\mathbf{U_p} = \boldsymbol{\alpha}$ of the theory of dislocations (Acharya, 2001). A point-wise measure of the translational incompatibility due to the presence of dislocations is the Burgers vector. The latter contains a possible contribution from disclinations and reads

$$\mathbf{b} = \int_C (\boldsymbol{\epsilon}_e-(\boldsymbol{\kappa}_e^t\times\mathbf{r})^t)\cdot\mathbf{dr} = \int_S (\boldsymbol{\alpha}-(\boldsymbol{\theta}\times\mathbf{r})^t)\cdot\mathbf{n}\,dS \tag{23}$$

Note that Eqs. (16) and (21) may be utilized to estimate the disclination and Nye's dislocation density tensors from EBSD experiments, respectively (Beausir and Fressengeas, in press). The continuity condition $\mathbf{div}\,\boldsymbol{\alpha}=0$ for dislocations is also modified when disclinations are present. Taking the divergence of Eq. (21) and defining the twist-disclination vector $\overrightarrow{\boldsymbol{\Theta}}$ as

$$\overrightarrow{\boldsymbol{\Theta}} = -\frac{1}{2}\boldsymbol{\theta}:\mathbf{X} \tag{24}$$

it is found that

$$\mathbf{div}\,\boldsymbol{\alpha}+2\overrightarrow{\boldsymbol{\Theta}} = 0 \tag{25}$$

This continuity equation implies the existence of geometric interactions between twist-disclinations ($i\neq j$) and dislocations.

In the absence of body forces, the rate form of the momentum and moment of momentum equations is

$$\mathbf{div}\,\dot{\mathbf{T}} = 0 \tag{26}$$

$$\mathbf{div}\,\dot{\mathbf{M}}+2\dot{\overrightarrow{\mathbf{T}}} = 0 \tag{27}$$

In these relations, the stress tensor $\mathbf{T}$ is generally non-symmetric. The skew-symmetric stress vector, $\overrightarrow{\mathbf{T}}$, defined as $\overrightarrow{\mathbf{T}} = -1/2\mathbf{T}:\mathbf{X}$, allows balancing the moment of momentum in the presence of the couple-stress tensor $\mathbf{M}$. A specific free

energy density function is now introduced as follows:

$$\psi = \psi(\boldsymbol{\epsilon}_e, \boldsymbol{\kappa}_e) \tag{28}$$

In addition to elastic strains, ψ contains contributions from the elastic curvatures when disclinations are present, *i.e.*, when incompatible elastic curvatures exist. Thus, the body is seen as a continuum containing capable of transmitting stresses and couple-stresses at nanometer scale. Differentiating Eq. (28), we obtain the following identification of the stress and couple-stress tensors with the partial derivatives of the free energy:

$$\dot{\psi} = \frac{\partial \psi}{\partial \boldsymbol{\epsilon}_e} : \dot{\boldsymbol{\epsilon}}_e + \frac{\partial \psi}{\partial \boldsymbol{\kappa}_e} : \dot{\boldsymbol{\kappa}}_e = \mathbf{T} : \dot{\boldsymbol{\epsilon}}_e + \mathbf{M} : \dot{\boldsymbol{\kappa}}_e \tag{29}$$

Owing to the symmetry of the elastic strain rate tensor, only the symmetric part $\mathbf{T}^{sym}$ of the stress tensor is contributing to the free energy. The elastic constitutive relations for $\mathbf{T}^{sym}$ and $\mathbf{M}$ are consistently chosen in the form suggested in DeWit (1970)

$$\mathbf{T}^{sym} = \mathbf{C} : \boldsymbol{\epsilon}_e + \mathbf{D} : \boldsymbol{\kappa}_e \tag{30}$$

$$\mathbf{M} = \mathbf{A} : \boldsymbol{\kappa}_e + \mathbf{B} : \boldsymbol{\epsilon}_e \tag{31}$$

The skew-symmetric part $\mathbf{T}^{skew}$ of the stress tensor is not involved in Eqs. (29) and (30) and is not constitutively specified. $\mathbf{A}$, $\mathbf{B}$, $\mathbf{C}$ and $\mathbf{D}$ are tensors of elastic constants. While the C_{ijkl} and A_{ijkl} constants have dimension of a stress and a stress times a squared length respectively, B_{ijkl} and D_{ijkl} have dimension of a stress multiplied by a length. Hence, the relations (30) and (31) involve characteristic lengths and have non-local character. Indeed, the tensor $\mathbf{D}$ induces stresses due to the inhomogeneity in rotation over some (short) length scale, while the tensor $\mathbf{B}$ gives rise to couple stresses from inhomogeneity in strain over some other (short) length scale. In the presence of crystal defects, a general form of the tensors $\mathbf{A}$, $\mathbf{B}$, $\mathbf{C}$ and $\mathbf{D}$ is derived in Upadhyay et al. (accepted), in the case of isotropic elasticity.

In terms of the plastic strain and curvature rates $\dot{\boldsymbol{\epsilon}}_p$ and $\dot{\boldsymbol{\kappa}}_p$, the stress rate and couple stress rate are

$$\dot{\mathbf{T}}^{sym} = \mathbf{C} : (\{\mathbf{grad}\, \dot{\mathbf{u}}\} - \dot{\boldsymbol{\epsilon}}_p) + \mathbf{D} : (\mathbf{grad}\, \vec{\dot{\boldsymbol{\omega}}} - \dot{\boldsymbol{\kappa}}_p) \tag{32}$$

$$\dot{\mathbf{M}} = \mathbf{A} : (\mathbf{grad}\, \vec{\dot{\boldsymbol{\omega}}} - \dot{\boldsymbol{\kappa}}_p) + \mathbf{B} : (\{\mathbf{grad}\, \dot{\mathbf{u}}\} - \dot{\boldsymbol{\epsilon}}_p) \tag{33}$$

In the presence of stress and couple-stress fields, the dislocation and disclination densities may be transported (set into motion) with respective velocities $\mathbf{V}_\alpha$ and $\mathbf{V}_\theta$. The driving Peach-Köhler-type forces $\mathbf{F}_\alpha$ and $\mathbf{F}_\theta$ acting on these defects are defined thermodynamically such that the power dissipation due to defect mobility is not negative (Fressengeas et al., 2011). In the simplest possible setting, linear viscosity is assumed and the dislocation and disclination velocities are taken as

$$\mathbf{V}_\alpha = \frac{\mathbf{F}_\alpha}{B_\alpha} = \frac{1}{B_\alpha} \mathbf{T}^{sym} \cdot \boldsymbol{\alpha} : \mathbf{X};\ V_l^\alpha = \frac{1}{B_\alpha} e_{jkl} \frac{T_{ij} + T_{ji}}{2} \alpha_{ik} \tag{34}$$

$$\mathbf{V}_\theta = \frac{\mathbf{F}_\theta}{B_\theta} = \frac{1}{B_\theta} \mathbf{M}^t \cdot \boldsymbol{\theta} : \mathbf{X};\ V_l^\theta = \frac{1}{B_\theta} e_{jkl} M_{ij} \theta_{ik} \tag{35}$$

Here, B_α and B_θ are positive drag coefficients. Eqs. (34) and (35) may be applicable at relatively high loading rate, but they need modification to account for thermally activated motion of defects typical at low loading rates. This issue will be discussed further in Section 6. Note that the dislocations are driven by the symmetric part of the stress tensor, while the disclinations are set into motion by the couple-stress field. The mobility of disclinations and dislocations produces the plastic curvature and strain rates:

$$\dot{\boldsymbol{\kappa}}_p = \boldsymbol{\theta} \times \mathbf{V}_\theta \tag{36}$$

$$\dot{\boldsymbol{\epsilon}}_p = \frac{1}{2} (\boldsymbol{\alpha} \times \mathbf{V}_\alpha + (\boldsymbol{\alpha} \times \mathbf{V}_\alpha)^t) \tag{37}$$

In turn, $\dot{\boldsymbol{\kappa}}_p$ and $\dot{\boldsymbol{\epsilon}}_p$ feed the evolution of the disclination and dislocation densities through the transport equations

$$\dot{\boldsymbol{\theta}} = -\mathbf{curl}\, \dot{\boldsymbol{\kappa}}_p \tag{38}$$

$$\dot{\boldsymbol{\alpha}} = -\mathbf{curl}\, \dot{\boldsymbol{\epsilon}}_p + \dot{\boldsymbol{\kappa}}_p^t - \mathrm{tr}(\dot{\boldsymbol{\kappa}}_p)\mathbf{I} = -\mathbf{curl}\, \dot{\boldsymbol{\epsilon}}_p + \mathbf{s}_\theta \tag{39}$$

Disclinations nucleate from the incompatibility of the plastic curvature rates in Eq. (38), but an outstanding consequence of Eq. (39) is that dislocations are nucleated not only because the plastic strain rate has an incompatible part, $\dot{\boldsymbol{\epsilon}}_p^{\perp}$, but also because a source term, $\mathbf{s}_\theta = \dot{\boldsymbol{\kappa}}_p^t - \mathrm{tr}(\dot{\boldsymbol{\kappa}}_p)\mathbf{I}$, involving the mobility of the disclinations is existing. Thus, a wake of dislocations (nucleated or absorbed) is accompanying the motion of disclinations. In contrast with the dislocations arising from lattice translational incompatibility (the curl term in Eq. (39)), this wake of dislocations may be seen as systematically contributing to the relaxation of internal stresses in the neighborhood of disclinations (Romanov and Vladimirov, 1992; Kleman and Friedel, 2008).

In the following, we develop further the rate form of the elasto-plastic theory of crystal defects proposed in the earlier paper (Fressengeas et al., 2011). The latter is contained in the set of Eqs. (26), (27), and (30)–(39). Solving the rate of

equilibrium Eqs. (26) and (27) involves finding the total strain rate and curvature rate tensors. As is well-known, the strain tensor is the symmetric part of the displacement gradient. Similarly, because it is the gradient of the rotation vector, the curvature tensor also derives from the displacement (see Eqs. (9) and (15)). Thus, the only independent kinematic variable in Eqs. (26) and (27) is the material velocity vector. Following Mindlin and Tiersten (1962), the three additional independent scalar variables necessary for closure (see *e.g.* (Shu et al., 1999)) are the components of the skew-symmetric part $\mathbf{T}^{skew}$ of the stress tensor. The latter is produced by the presence of unbalanced couple stresses and ensures the balance of moment of momentum (Mindlin and Tiersten, 1962; Hadjesfandiari and Dargush, 2011). Taking the curl of Eq. (27) and eliminating $\mathbf{T}^{skew}$ in Eq. (26), the latter can be rewritten as a single higher order partial differential equation for the total velocity field

$$\mathbf{div}\,\dot{\mathbf{T}} = \mathbf{div}\,\dot{\mathbf{T}}^{sym} + \mathbf{div}\,\dot{\mathbf{T}}^{skew} = \mathbf{div}\,\dot{\mathbf{T}}^{sym} + \frac{1}{2}\,\mathbf{curl}\,\mathbf{div}\,\dot{\mathbf{M}} = 0 \tag{40}$$

In terms of the elastic strains and curvatures, Eq. (40) reads

$$\mathbf{div}(\mathbf{C} : \dot{\boldsymbol{\epsilon}}_e + \mathbf{D} : \dot{\boldsymbol{\kappa}}_e) + \frac{1}{2}\,\mathbf{curl}\,\mathbf{div}(\mathbf{A} : \dot{\boldsymbol{\kappa}}_e + \mathbf{B} : \dot{\boldsymbol{\epsilon}}_e) = 0 \tag{41}$$

Substituting the total and plastic strain and curvature rates to their elastic counterparts in Eq. (41), we obtain

$$\mathbf{div}(\mathbf{C} : (\dot{\boldsymbol{\epsilon}} - \dot{\boldsymbol{\epsilon}}_p) + \mathbf{D} : (\dot{\boldsymbol{\kappa}} - \dot{\boldsymbol{\kappa}}_p)) + \frac{1}{2}\,\mathbf{curl}\,\mathbf{div}(\mathbf{A} : (\dot{\boldsymbol{\kappa}} - \dot{\boldsymbol{\kappa}}_p) + \mathbf{B} : (\dot{\boldsymbol{\epsilon}} - \dot{\boldsymbol{\epsilon}}_p)) = 0 \tag{42}$$

The rate form of the elasto-plastic theory of crystal defects is then defined by the set of Eqs. (34)–(39) and (42). The unknown fields are the material velocity, dislocation and disclination density fields. The set up of initial and boundary conditions, the numerical scheme will be described below.

4. A plane edge-wedge model

The plane edge-wedge model presented in this section was introduced in Fressengeas et al. (2011). It is recalled briefly here for completeness. Let us consider a distribution of pure wedge disclinations. In an orthonormal reference frame $(\mathbf{e_1},\mathbf{e_2},\mathbf{e_3})$, let the disclination tensor be: $\boldsymbol{\theta} = \theta_{33}\mathbf{e_3}\otimes\mathbf{e_3}$, all other components being zero. In this simple setting, the continuity condition (20) implies: $\theta_{33,3} = 0$. Thus, the wedge disclination density θ_{33} only depends on the coordinates (x_1,x_2) : $\theta = \theta(x_1,x_2)$. In component form, the rotational incompatibility Eq. (16) reads: $\theta_{ij} = -e_{jkl}\kappa^p_{il,k} = e_{jkl}\kappa^e_{il,k}$. In the present case, Eq. (16) reduces to

$$\theta_{33} = \kappa^p_{31,2} - \kappa^p_{32,1} = \kappa^e_{32,1} - \kappa^e_{31,2} \tag{43}$$

Hence the only relevant elastic and plastic curvatures are: $(\kappa^e_{31},\kappa^e_{32})$ and $(\kappa^p_{31},\kappa^p_{32})$. Additionally, we note that: $\mathrm{tr}(\boldsymbol{\kappa}_p) = 0$. Thus, the disclination transport Eq. (38) is

$$\dot{\theta}_{33} = \dot{\kappa}^p_{31,2} - \dot{\kappa}^p_{32,1} \tag{44}$$

The plastic curvature rate (36) reads, in component form: $\dot{\kappa}^p_{ij} = e_{jkl}\theta_{ik}V^\theta_l$. Hence, we find

$$\dot{\kappa}^p_{31} = -\theta_{33}V^\theta_2 \tag{45}$$

$$\dot{\kappa}^p_{32} = +\theta_{33}V^\theta_1 \tag{46}$$

Using the constitutive relation (35) for the disclination velocities provides their relationship with the couple-stresses

$$V^\theta_1 = +\frac{1}{B_\theta}M_{32}\theta_{33} \tag{47}$$

$$V^\theta_2 = -\frac{1}{B_\theta}M_{31}\theta_{33} \tag{48}$$

Since the trace of the plastic curvature rate tensor is zero, the source term $\mathbf{s}_\theta$ in the dislocation transport Eq. (39) feeds only the edge dislocations densities $(\alpha_{13},\alpha_{23})$. Using Eq. (37), it is seen that the motion of these dislocations produces the plastic strain rate components $(\dot{\epsilon}^p_{11},\dot{\epsilon}^p_{12},\dot{\epsilon}^p_{21},\dot{\epsilon}^p_{22})$

$$\dot{\epsilon}^p_{11} = -\alpha_{13}V^\alpha_2 \tag{49}$$

$$\dot{\epsilon}^p_{12} = \dot{\epsilon}^p_{21} = \tfrac{1}{2}(\alpha_{13}V^\alpha_1 - \alpha_{23}V^\alpha_2) \tag{50}$$

$$\dot{\epsilon}^p_{22} = +\alpha_{23}V^\alpha_1 \tag{51}$$

The above relations suggest that out-of-plane motion of the edge dislocations $(\alpha_{13},\alpha_{23})$ is involved in the extension rates $(\dot{\epsilon}^p_{11},\dot{\epsilon}^p_{22})$, whereas their glide is responsible for $\dot{\epsilon}^p_{12}$. Consistently, the dislocation transport Eq. (39) reduces to

$$\dot{\alpha}_{13} = \dot{\epsilon}^p_{11,2} - \dot{\epsilon}^p_{12,1} + \dot{\kappa}^p_{31} \tag{52}$$

$$\dot{\alpha}_{23} = \dot{\epsilon}^p_{21,2} - \dot{\epsilon}^p_{22,1} + \dot{\kappa}^p_{32} \tag{53}$$

Thus, if all other dislocation densities are initially absent, the dislocation distribution involves only α_{13} and α_{23} edge densities. The continuity Eq. (25) then implies that this distribution be a plane state: $\alpha_{13} = \alpha_{13}(x_1,x_2), \alpha_{23} = \alpha_{23}(x_1,x_2)$. The symmetric "Peach-Köhler" constitutive relation (34) provides the dislocation velocities in terms of the stress tensor, for both the out-of-plane motion of dislocations

$$V^\alpha_1 = +\frac{1}{B_\alpha} T_{22}\alpha_{23} \tag{54}$$

$$V^\alpha_2 = -\frac{1}{B_\alpha} T_{11}\alpha_{13} \tag{55}$$

and their glide

$$V^\alpha_1 = +\frac{1}{2B_\alpha} (T_{12}+T_{21})\alpha_{13} \tag{56}$$

$$V^\alpha_2 = -\frac{1}{2B_\alpha} (T_{12}+T_{21})\alpha_{23} \tag{57}$$

The stress and couple-stress components relevant to the present problem are $(T_{11},T_{12},T_{21},T_{22})$ and (M_{31},M_{32}) respectively. Hence the Cosserat rate of momentum Eqs. (26) and (27) reduce to

$$\dot{T}_{11,1} + \dot{T}_{12,2} = 0 \tag{58}$$

$$\dot{T}_{21,1} + \dot{T}_{22,2} = 0 \tag{59}$$

$$\dot{M}_{31,1} + \dot{M}_{32,2} + \dot{T}_{21} - \dot{T}_{12} = 0 \tag{60}$$

and the higher order rate of equilibrium Eq. (40) becomes

$$\dot{T}^{sym}_{11,1} + \dot{T}^{sym}_{12,2} + \dot{T}^{skew}_{12,2} = \dot{T}^{sym}_{11,1} + \dot{T}^{sym}_{12,2} + \frac{1}{2}(\dot{M}_{31,1} + \dot{M}_{32,2})_{,2} = 0 \tag{61}$$

$$\dot{T}^{sym}_{21,1} + \dot{T}^{skew}_{21,1} + \dot{T}^{sym}_{22,2} = \dot{T}^{sym}_{21,1} + \dot{T}^{sym}_{22,2} - \frac{1}{2}(\dot{M}_{31,1} + \dot{M}_{32,2})_{,1} = 0 \tag{62}$$

As shown in Fressengeas et al. (2011), the elastic tensor $\boldsymbol{B}$ is zero in a plane strain formulation. Thus, the symmetric stress components write

$$T^{sym}_{11} = C_{1111}\epsilon^e_{11} + C_{1122}\epsilon^e_{22} \tag{63}$$

$$T^{sym}_{12} = C_{1212}\epsilon^e_{12} + C_{1221}\epsilon^e_{21} \tag{64}$$

$$T^{sym}_{21} = C_{2112}\epsilon^e_{12} + C_{2121}\epsilon^e_{21} \tag{65}$$

$$T^{sym}_{22} = C_{2211}\epsilon^e_{11} + C_{2222}\epsilon^e_{22} \tag{66}$$

with $C_{1212} = C_{1221} = C_{2112} = C_{2121}$, $C_{1111} = C_{2222}$ and $C_{1122} = C_{2211}$ in cubic symmetry. For convenience, a simplified form of tensor $\boldsymbol{A}$ will be used

$$M_{31} = A_{3131}\kappa^e_{31} \tag{67}$$

$$M_{32} = A_{3232}\kappa^e_{32} \tag{68}$$

The coefficients C_{ijkl} may be determined from experiments or by atomistic simulations. In the forthcoming simulations, we shall use values for copper, as determined by molecular dynamics simulations (Spearot, 2005). In addition, we assume $A_{3131} = A_{3232} = M\mu b^2$. Provisionally, we adopt the value $M=1$, consistent with an earlier estimate (Kröner, 1963). The ratio A_{3131}/μ introduces a characteristic squared length $l^2 = b^2$ in the balance of momentum Eq. (42). This internal length l should be the order of the smallest microstructure characteristic size and respect the small strain hypothesis in terms of curvatures $|\kappa_{ij}| < 1/l$ (Hadjesfandiari and Dargush, 2011). In the present framework of GB modeling at a sub-atomic resolution scale, $l=b$ is a reasonable upper bound value. Further, we assume equal viscous drag coefficients $B_\theta = B_\alpha = B$. The mobility of the disclinations might be overestimated by doing so, but this value conveniently allows showing the features of disclination dynamics in the following. A more accurate value of B_θ will be derived from grain boundary migration data in future work. Parameter values for copper are presented in Table 1.

Substituting Eqs. (63)–(68) and $(\dot{\epsilon}_{ij} - \dot{\epsilon}^p_{ij}, \dot{\kappa}_{ij} - \dot{\kappa}^p_{ij})$ for the elastic strain and curvature rates in the equilibrium Eqs. (61) and (62), one obtains two partial differential equations for the material velocity field (v_1,v_2). The plastic strains and curvatures and the disclination and dislocation densities are updated using the plastic strain and curvature rates (45), (46), and (49)–(51), and the transport Eqs. (44), (52), and (53) respectively. The boundary conditions for the equilibrium problem comprise the prescription

Table 1
Numerical constants used in the model.

b	C_{1212}	C_{1111}	C_{1122}	b^2B	M
0.25 nm	27 GPa	175 GPa	125 GPa	0.4×10^{-4} Pa s	1

of tractions and traction-moments, or/and displacements and rotations on the surface of the body. The equilibrium equations are solved using a Galerkin finite element method, with 16-nodes complete cubic elements for the interpolation of the material velocity field, and 16 Gauss points for the integration. The transport equations are solved using a Least-Squares finite element scheme (Varadhan et al., 2006) with bilinear elements for the interpolation of dislocation and disclination densities, and four Gauss points for the integration. Note that a cubic element contains nine bilinear elements such that the material velocity, the dislocation and disclination densities are discretized at the same nodes in the finite element mesh. Finally, the disclination and dislocation densities need to be specified on inflow boundaries, but no condition is required on outflow boundaries. The set up of initial conditions is presented in the next section.

In order to compare our continuous orientation predictions with crystalline orientations, we compute the compatible elastic rotation about the tilt axis. As already mentioned in Section 3, the elastic rotation does not exist in the present crystal defect theory. In other words, it cannot be integrated from the elastic curvature tensor, because the latter contains an incompatible part. However, a compatible elastic rotation can be defined by integrating the compatible part of the elastic curvature tensor. In components form, the latter is known from the plastic and total curvature tensors as

$$\kappa^{e\|}_{ij}=\kappa^{e}_{ij}-\kappa^{e\perp}_{ij}=\kappa^{e}_{ij}+\kappa^{p\perp}_{ij} \tag{69}$$

where the plastic curvatures are obtained from Eqs. (72) and (73) (recall that the incompatible elastic curvatures are opposed to their plastic counterparts to ensure that the total curvatures remains compatible). Then, the compatible elastic rotation $\omega^{e\|}_3$ is solution to the system

$$\omega^{e\|}_{3,1}=\kappa^{e\|}_{31} \tag{70}$$

$$\omega^{e\|}_{3,2}=\kappa^{e\|}_{32} \tag{71}$$

5. Initial conditions for grain boundaries

In the DSUM (Gertsman et al., 1989), tilt boundaries are modeled as periodic walls of discrete wedge disclination dipoles. Dislocations are absent from this representation. In this section, our aim is to implement initial conditions for the evolution of the disclination density by mimicking the disclination dipole walls from the DSUM through elasto-static calculations. Thus, a continuous wedge disclination density θ_{33} is first prescribed, with periodic boundary conditions in the x_1 direction to model an infinite wall of dipoles along this direction. We note that even if prescribed at a single node to be as close as possible to the discrete disclinations envisioned in the DSUM, the initial disclination density remains continuous in the present work, due to the finite element interpolation. Assuming incompatibility of the initial plastic curvatures, Eq. (17) must be satisfied, together with the side conditions $\mathbf{div}\,\boldsymbol{\kappa}^{\perp}_{p}=0$ and $\boldsymbol{\kappa}^{\perp}_{p}\cdot\mathbf{n}=0$ on the boundary with unit normal $\mathbf{n}$. It can be easily shown that the plastic curvatures then satisfy the following equations:

$$\kappa^{p\perp}_{31,11}+\kappa^{p\perp}_{31,22}=\theta_{33,2} \tag{72}$$

$$\kappa^{p\perp}_{32,11}+\kappa^{p\perp}_{32,22}=-\theta_{33,1} \tag{73}$$

We solve the above system of equations using a Galerkin finite element scheme with bilinear elements and with Lagrange multipliers to enforce $\boldsymbol{\kappa}^{\perp}_{p}\cdot\mathbf{n}=0$ on the boundaries. Since the plastic curvatures are incompatible, the initial total curvature tensor coincides with the compatible part of the elastic curvature tensor, as given by the equilibrium equations. Now, in order to mimic the DSUM dipole walls, we look for initial plastic strains such that the edge dislocation densities α_{13} and α_{23} be zero. Assuming again incompatibility of the initial plastic strain, it is seen from Eqs. (52) and (53) that the latter must be solution to the following equations:

$$\epsilon^{p\perp}_{11,2}-\epsilon^{p\perp}_{12,1}=-\kappa^{p}_{31} \tag{74}$$

$$\epsilon^{p\perp}_{21,2}-\epsilon^{p\perp}_{22,1}=-\kappa^{p}_{32} \tag{75}$$

augmented with the side conditions $\mathbf{div}\,\boldsymbol{\epsilon}^{\perp}_{p}=0$ and $\boldsymbol{\epsilon}^{\perp}_{p}\cdot\mathbf{n}=0$ on the boundary with unit normal $\mathbf{n}$. The following set of equations is then derived:

$$\epsilon^{p\perp}_{11,11}+\epsilon^{p\perp}_{11,22}=-\kappa^{p}_{31,2} \tag{76}$$

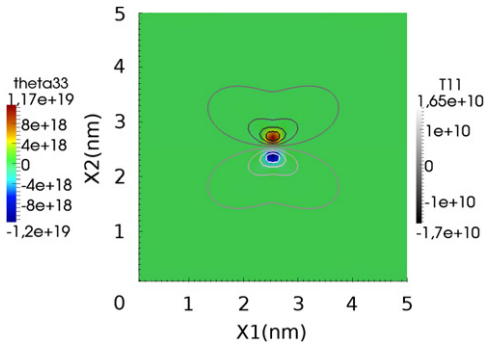

Fig. 1. Initial wedge disclination dipole of Frank vector ± 0.75 rad and arm length 0.25 nm. The disclination density θ_{33} is shown in rad m^{-2} units. Superimposed is the contour plot of the T_{11}^{sym} tensile stress component (in Pa units). The simulation box is a 5 nm $\times$ 5 nm square containing 20×20 cubic elements for the Galerkin finite element scheme for equilibrium, and 60×60 bilinear elements for the Least-Squares transport scheme.

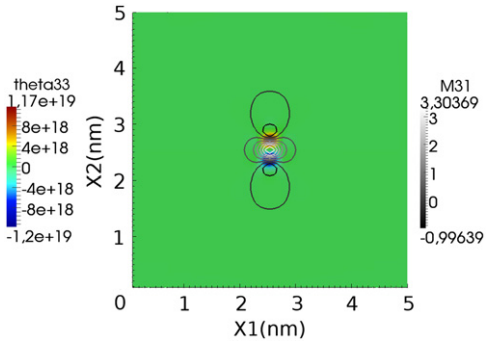

Fig. 2. Initial wedge disclination dipole of Frank vector ± 0.75 rad and arm length 0.25 nm. The disclination density θ_{33} is shown in rad m^{-2} units. Superimposed is the contour plot of the M_{31} couple stress component (in Pa m units). The simulation box is a 5 nm $\times$ 5 nm square containing 20×20 cubic elements for the Galerkin finite element scheme for equilibrium, and 60×60 bilinear elements for the Least-Squares transport scheme.

$$\epsilon_{22,11}^{p\perp} + \epsilon_{22,22}^{p\perp} = \kappa_{32,1}^{p} \tag{77}$$

$$\epsilon_{12,11}^{p\perp} + \epsilon_{12,22}^{p\perp} = \kappa_{31,1}^{p} = -\kappa_{32,2}^{p} \tag{78}$$

Similarly to Eqs. (72) and (73), Eqs. (76)–(78) are solved using a Galerkin finite element scheme with bilinear elements and with Lagrange multipliers to enforce $\boldsymbol{\epsilon}_p^{\perp} \cdot \mathbf{n} = 0$ on the boundaries. Then, as a consequence of Eqs. (10) and (22), the incompatible part of the elastic strain tensor automatically satisfies Eq. (21). Finally, the compatible part of the initial elastic strain tensor is found from the solution of the equilibrium equations.

In order to validate the above layout of initial conditions, a single disclination dipole aligned with the x_2 direction is simulated. The simulation area is a 5 nm $\times$ 5 nm square box containing 20×20 cubic elements for the Galerkin finite element scheme for equilibrium, and 60×60 bilinear elements for the Least-Squares transport scheme. Thus, the length of a cubic element is 0.25 nm, the order of the Burgers vector magnitude b in copper. The shortest distance between nodes is approximately 0.83 Å, lower than interatomic distances. The material displacements are free and no traction is applied on boundaries normal to the x_2 direction, whereas periodicity is assumed on boundaries normal to the x_1 direction. The resulting disclination dipole is shown in Figs. 1 and 2. Its arm length is the order of b. Its strength, determined by the Frank vector, is ± 0.75 rad. The tensile stress component T_{11}^{sym} is shown in Fig. 1. As expected, the stress/strain field of the disclination dipole is close to that of an equivalent discrete edge dislocation of Burgers vector along the x_1 axis and line direction along the x_3 axis in a infinite medium (see *e.g.* Upadhyay et al., 2011), although the simulation box is finite in one direction and periodic in the other direction. A beneficial feature of the present scheme is that the stresses are regularized in the core region because the disclination and dislocation densities are continuous quantities. Another benefit is that the couple-stress/curvature field is better described than in a pure edge dislocation representation. Indeed, the incompatible part of the elastic curvature, altogether absent in the theory of dislocations, is accounted for in the present solution. As an illustration, the couple-stress field M_{31} of the simulated dipole is shown in Fig. 2. It is essentially due to the incompatible elastic curvature $\kappa_{31}^{e\perp}$. Not apparent in the above, another substantial difference with static models is that, driven by its own couple-stress field, the disclination dipole shown in Fig. 2 is set into motion. Indeed, it can be seen from the superposition of the disclination density and couple stress fields in Fig. 2, that the driving forces and velocities involved in

Eqs. (47) and (48) are non-zero over a large overlapping area. This feature strongly suggests that the disclination dipoles considered in static models may not necessarily be stable, and that allowing their transport should lead to self-organized relaxed configurations.

We now focus on setting up $\langle 001 \rangle$ symmetric tilt boundaries in copper. Used as a benchmark hereafter, the DSUM is briefly recalled for convenience. Based on atomistic computer simulations, the Structural Unit Model (SUM) was first proposed by Sutton and Vitek (1983). For a given misorientation axis, there exist several tilt boundaries built with periodic arrangements of only one type of atomic structural units, and referred to as "favored boundaries". For the $\langle 001 \rangle$ axis in fcc copper, four such tilt boundaries are existing. They are made of A, B, C or D units and correspond to 0°, 36.87°, 53.13°, and 90° misorientations, respectively (we use the conventions of Bachurin et al., 2003 hereafter). For misorientations lying in a range between two favored boundaries, the tilt boundary consists in a periodic sequence composed of the two structural units associated with the bounding favored boundaries. In these mixed sequences, minority and majority units are referred to as the less and more frequent units, respectively. The DSUM is based on the idea that each structural unit is equivalent to a discrete wedge disclination dipole (Gertsman et al., 1989), whose strength (Frank vector) is the misorientation of the associated favored boundary, and whose arm length is the structural unit length. As there is no spacing between the discrete disclination dipoles in their periodic arrangement, the Frank vectors of disclinations coexisting at the same point are added in the DSUM. Hence, the DSUM periodic configurations produce a relative misorientation with respect to the closest favored boundary. In particular, the 36.87° and 53.13° misorientations of the favored boundaries cannot be retrieved because the Frank vectors of adjacent dipoles exactly cancel. In the range 0–22.62° where grain boundaries are made of A majority and B minority units, dipoles with polar strength $\langle -36.87, +36.87 \rangle$ degrees are used and give a misorientation θ with respect to 0°. In the range 64.94–90° where grain boundaries are made of C minority and D majority units, dipoles with polar strength $\langle +36.87, -36.87 \rangle$ degrees are used. They give a misorientation θ with respect to 90°, equivalent to a misorientation $90-\theta$ with respect to 0°. In these ranges only, the DSUM provides absolute misorientations. However, in the range 22.62–64.94°, misorientations are relative to either 36.87° or 53.13°. The construction of dipole sequences for the full range of misorientations can be found in Upadhyay et al. (2011). Initial configurations based on the DSUM, referred to as configurations (a) hereafter, will be relaxed in the next section, using our edge-wedge model. Specifically, initially confined disclination densities will be set-up such that the strengths and the dipole arm lengths and spacings are those of the DSUM.

Construction schemes other than the DSUM can be proposed for reproducing a tilt boundary with a given misorientation. In configuration (b) now described, we aim at modeling absolute misorientations in the full range 0–90°. To overcome the relative character of the DSUM in the range 22.62–64.94°, we propose a scheme based on the geometrical duality of the B and C units (by geometrical duality we mean complementarity of the misorientations: $36.87 + 53.13 = 90°$): A dipole B with polar strength $\langle -36.87, +36.87 \rangle$ degrees, which tends to produce a misorientation of 36.87° with respect to 0°, may be replaced by a dipole of same arm length but with polar strength $\langle +53.13, -53.13 \rangle$ degrees, referred to as C^-. The latter tends indeed to produce a misorientation of 53.13° with respect to 90°, equivalent to a misorientation of $90-53.13 = 36.87°$ with respect to 0 degree. Similarly, a disclination dipole C of polar strength $\langle -53.13, +53.13 \rangle$ degrees may be replaced with a dipole of same arm length but with polar strength $\langle +36.87, -36.87 \rangle$ degrees, referred to as B^-. As an illustration, the $B{-}B{-}B{-}B$ periodic structure of the 36.87° favored boundary may be replaced by a $B{-}C^-{-}B{-}C^-$ periodic sequence. The latter is then modeled by dipoles with polar strength $\langle -90, +90 \rangle$ degrees, with arm length and spacing both equals to the length of B units. In configuration (b), the initial dipole arm lengths and spacings are still corresponding to atomic structural units, as in the DSUM. However, the initial Frank vectors are different. They now have very high magnitude, and as will be seen in the next section, relaxation by transport of the disclination dipoles in their own couple-stress field leads to smaller Frank vectors and periodic sequences converging towards the correct misorientation.

It is expected that the elastic energy of configurations (b) should be closer to molecular statics data than that of configurations (a). Indeed, it is only by assigning conveniently chosen energy values to the 36.87° and 53.13° favored boundaries, that the DSUM does retrieve molecular statics energy levels while getting only relative misorientations. In future work, other initial structural unit-based configurations will be proposed and analyzed in comparison with molecular dynamics simulations, to possibly identify the most appropriate way to build grain boundaries. For the purpose of illustrating the predictive capabilities of our model in terms of misorientation and energy level however, we believe that relaxing configurations (a) and (b) is sufficient.

6. Relaxation of tilt boundaries

In all forthcoming simulations, the relaxation of initial configurations will be stopped when the driving forces for the motion of disclinations and dislocations reach a limiting value. The common threshold value of 5 MPa/$b = 2.10^{19}$ Pa/m was used for both disclinations (in plane and out-of-plane motions) and dislocations. If the relaxation process was not interrupted, the disclination densities would finally vanish from the simulation box after annihilation and spreading over a sufficiently long computation time. This feature originates in the linear viscous drag velocity laws (34) and (35) currently assumed in the model for the mobility of dislocations and disclinations. The value of the drag coefficient was checked to have an effect solely on the time needed for relaxation, but does not affect the relaxed structure and energy of grain

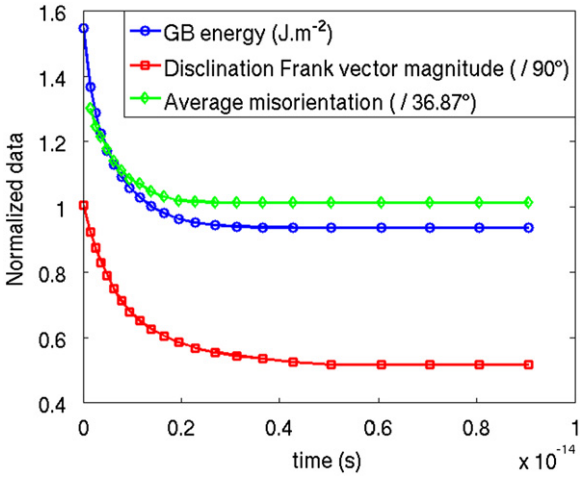

Fig. 3. Relaxation in time of a $\langle 001 \rangle \Sigma 5(210)$ tilt boundary of misorientation 36.87° using construction method (b).

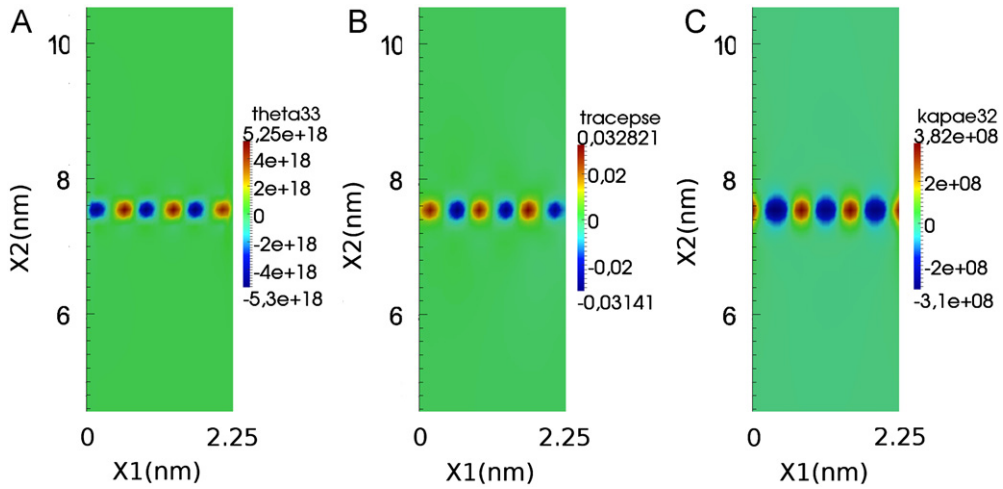

Fig. 4. Relaxed $\langle 001 \rangle \Sigma 29(520)$ tilt boundary of misorientation 46.40° using construction method (a). The simulation box is a 2.25 nm × 15 nm plane containing 9 × 60 cubic elements for the Galerkin finite element scheme for equilibrium, and 27 × 180 bilinear elements for the Least-Squares transport scheme. Closing-up is performed in the vertical direction. (A) Disclination dentity θ_{33} in rad m^{-2} units. (B) Trace of elastic strain tensor. (C) Elastic curvature κ^e_{32} (rad m^{-1}).

boundaries. Thus, the small relaxation times shown in Fig. 3 do not have a quantitative sense. As already mentioned, a thermally activated law featuring a threshold stress/couple stress would also alleviate indefinite relaxation in time.

Before comparing configurations (a) and (b) in detail, our interest is in validating configurations (b). Fig. 3 shows the relaxation in time of the initial configuration set out for a $\langle 001 \rangle \Sigma 5(210)$ tilt boundary. The figure shows that the initial Frank vector of the disclinations is halved in the self-organization process, which consists of spatial rearrangement and partial annihilation of the disclination densities, and nucleation of dislocations. Strikingly, the average elastic misorientation, *i.e.*, the difference in the compatible elastic rotation $\omega_3^{e\|}$ taken away from each side of the grain boundary, decreases from a high initial value and converges towards the correct value of 36.87°. The elastic energy of the grain boundary follows the same trend. Its relaxed value is 0.94 J m^{-2}, close to the molecular statics data for copper (Bachurin et al., 2003). Thus, configuration (b) is found to be rather realistic, but only after their relaxation by transport removes the initial arbitrariness in terms of disclination distribution and strength.

We now compare the relaxation of configurations (a) and (b) set out for a $\langle 001 \rangle \Sigma 29(520)$ tilt boundary (expected misorientation 46.40°). This boundary consists in a periodic sequence of alternating structural units B and C, initially represented by disclination dipoles of strength 36.87° and 53.13° and arm length 0.28 and 0.4 nm, respectively. Three dipoles were included in the simulation box. The relaxed structure obtained from configuration (a) is shown in Figs. 4 and 5. A wealth of features emerges from the simulations. The elastic strain field shows alternatively dilatation and contraction of the lattice along the boundary, in patches a few Å wide along the boundary also featuring the presence of negative and positive disclinations, respectively. This distribution is in good agreement with molecular statics predictions

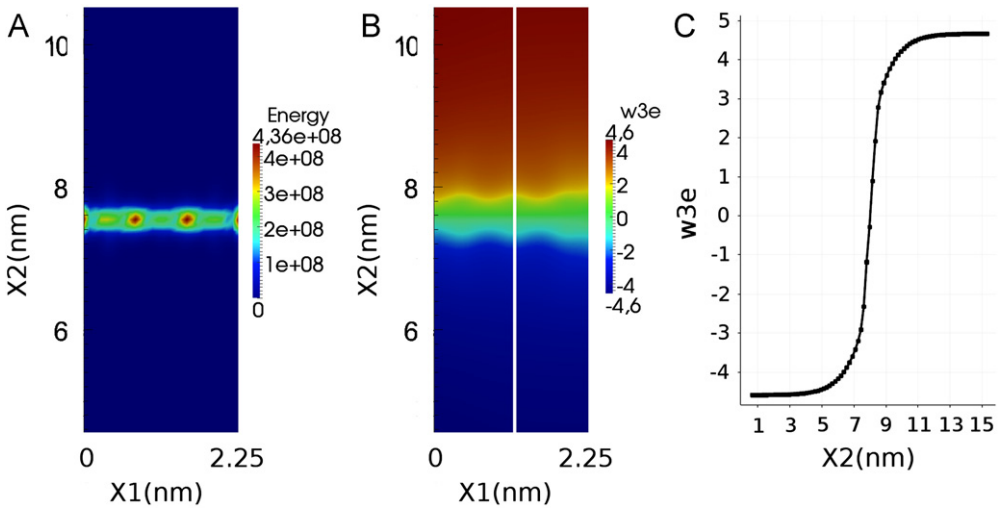

Fig. 5. Relaxed $\langle 001 \rangle \Sigma 29(520)$ tilt grain boundary of misorentation 46.40° using construction method (a). The simulation box is a 2.25 nm × 15 nm plane containing 9 × 60 cubic elements for the Galerkin finite element scheme for equilibrium, and 27 × 180 bilinear elements for the Least-Squares transport scheme. Close-up in vertical direction for figures (A) and (B). (A) Elastic energy density in J m^{-3} units. (B) Compatible elastic rotation ω_3^{el} around the tilt axis, in degree units. (C) Profile of the compatible elastic rotation all along the white line crossing (B). Rotation in degrees, all distances in nm.

(Sutton and Vitek, 1983). Between these patches, alternatively negative and positive curvature regions show up in the dipole interiors and between the dipoles respectively. The mobility of the disclinations was negligible during relaxation because of their small initial Frank vectors (16.26°). As a result, the relaxed distribution of disclinations remains localized and almost no edge dislocations were nucleated. The compatible elastic rotation is shown in Fig. 5. Remarkably, a quasi-uniform orientation is obtained on both sides of the dipole array. Hence, introducing a periodic wall of disclination dipoles in a single crystal amounts to creating a tilt boundary. The misorientation converges towards 9.2°. Recall that this misorientation is relative to the 36.87° favored boundary, which leads fairly correctly to the expected absolute misorientation of 46.40°. Note that the compatible elastic rotation evolves continuously across the grain boundary and is fully resolved by the finite element solution, although the 9.2° misorientation is occurring in a layer as thin as 1 nm. As a result, most of the elastic energy in the boundary area is also localized in this layer (see Fig. 5). This energy reflects both the translational and rotational incompatibility associated with the disclination dipole wall. The present model is therefore able to provide a realistic non-singular description of the grain boundary structure and energy. The energy density per unit length of boundary is 0.05 J m^{-2}. Because it corresponds to a relative misorientation, this value is unsurprisingly low.

The initial periodic sequence (b) consisting in dipoles with Frank vectors 106.26°, arm length 0.4 nm and spacing 0.28 nm, set up for the generation of a 46.40° tilt boundary, is now investigated. Its relaxed structure is shown in Fig. 6. As their initial Frank vector is large, significant mobility of the disclinations is seen during the relaxation. Their spatial rearrangement leads to spreading disclination densities and to decreasing values of the Frank vectors, due to partial annihilation. As a result, the relaxed distribution of disclinations is much more extended than that of configuration (a). Further, the misorientation now converges towards the absolute value 46°, very close to the expected value. Edge dislocations α_{13} and α_{23} are also nucleated during the process. These dislocations relax the initial stress field through both in-plane glide and out-of-plane motion, possibly through climb or atom shuffling. The resulting Burgers vector field is shown in Fig. 6. As suggested by a rotating pattern about the disclination dipoles, it is in close correlation with the disclination distribution. The net overall Burgers vector of the interface area is found to be zero, as could be expected from the absence of a discontinuity in the elastic strain and curvature tensors far away from the interface.[1] The elastic strain, curvature and energy fields are similar to their counterparts in configuration (a), but with higher levels. Again, most of the elastic energy is localized in a 1 nm layer, and the energy density per unit length of boundary is now 1 J m^{-2}, a value comparing rather well with that obtained from molecular statics calculations (Bachurin et al., 2003). Shown in Fig. 6B, the trace of the total strain tensor in the deformed mesh reflects the structure of the grain boundary. Remarkably, a translational asymmetry of the positive and negative disclinations is observed along the boundary. The overall structure of the interface area exhibits geometrical patterns showing clear similarities with the "kite-shaped" structural units of atomistic representations. Sections of the stress, elastic curvature and energy fields across and along the boundary are shown in Figs. 7 and 8, respectively. The contributions to the elastic energy of tension/compression strain and curvature

[1] It is found from Frank's formula that the separation distance l between the edge dislocations in a dislocation-made tilt boundary of misorientation 46.40° is $l = 0.34$ nm, a distance much too short to be realistic. Such a result supports the view that a consistent description of high-angle tilt boundaries should recourse to disclination dipole walls rather than edge dislocation walls.

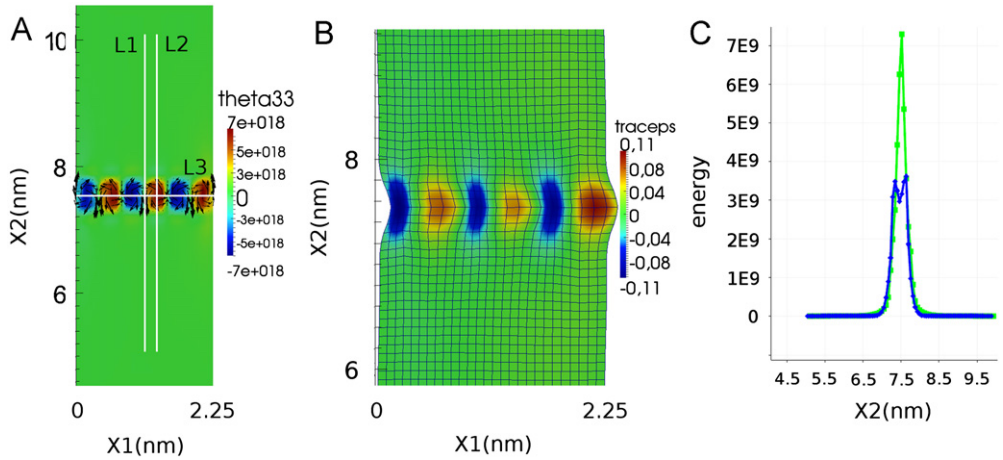

Fig. 6. Relaxed $\langle 001 \rangle \Sigma 29(520)$ tilt boundary of misorientation 46.40° using construction method (b). The simulation box is a 2.25 nm × 15 nm plane containing 9×60 cubic elements for the Galerkin finite element scheme for equilibrium, and 27×180 bilinear elements for the Least-Squares transport scheme. Close-up in vertical direction for figures (A) and (B). (A) Color-coded is the disclination density θ_{33} in rad m^{-2} units. Arrows show the orientation and the magnitude of the net Burgers vector due to edge dislocations. The maximum length of the Burgers vector corresponds to a density of 9×10^8 m^{-1}. (B) Trace of total strain tensor in the deformed mesh (displacements are magnified by a factor 5). (C) Profiles of elastic energy density (J m^{-3}) along white lines L1 (blue diamonds) and L2 (green squares) plotted in (A). (For interpretation of the references to color in this figure caption, the reader is referred to the web version of this article.)

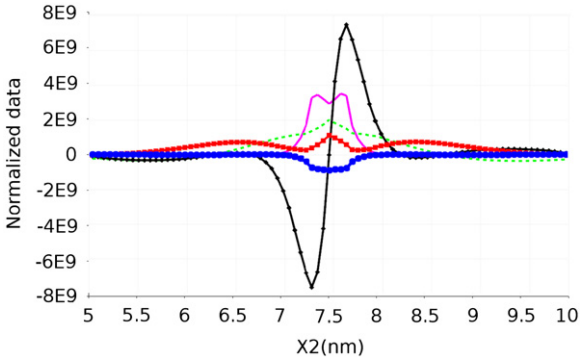

Fig. 7. Profiles across a disclination dipole (white line L1 in Fig. 6A) in the relaxed $\langle 001 \rangle \Sigma 29(520)$ tilt boundary of misorientation 46.40° using construction method (b) shown in Fig. 6. Energy density (J m^{-3}) in purple solid line, stress T_{11}^{sym} (Pa) in green dotted line, stress T_{12}^{sym} (Pa) in black diamond line, stress T_{22}^{sym} (Pa) in red square line and elastic curvature $\{\kappa_{32}^{e}\}$ (rad/m) in blue circle line. (For interpretation of the references to color in this figure caption, the reader is referred to the web version of this article.)

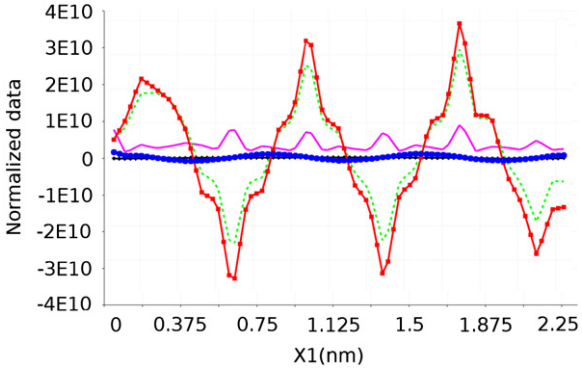

Fig. 8. Profiles along the grain boundary (white line L3 in Fig. 6A) in the relaxed $\langle 001 \rangle \Sigma 29(520)$ tilt boundary of misorientation 46.40° using construction method (b) shown in Fig. 6. Energy density (J m^{-3}) in purple solid line, stress T_{11}^{sym} (Pa) in green dotted line, stress T_{12}^{sym} (Pa) in black diamond line, stress $T_{22}^{sym}(Pa)$ in red square line and elastic curvature $\{\kappa_{32}^{e}\}$ (rad/m) in blue circle line. (For interpretation of the references to color in this figure caption, the reader is referred to the web version of this article.)

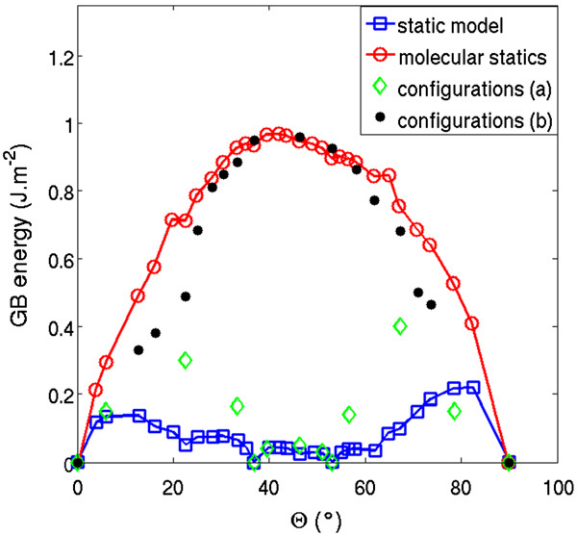

Fig. 9. Elastic energy density per unit length of grain boundary (J m^{-2}) obtained from relaxation of configurations (a) and (b). Molecular statics data for copper are shown for comparison (points were digitized from Bachurin et al., 2003). Predictions of a recent discrete DSUM-based static model are also shown (points were retrieved from Upadhyay et al., 2011).

are inter-twinned and correlated with disclination-rich and disclination-poor patches respectively. The tensile stress can reach values as high as 35 GPa, *i.e.*, it is on the order of the shear modulus in copper. Such large values were reported for the hydrostatic stress in structural units by atomistic simulations (Sutton and Vitek, 1983). The tensile/compressive elastic energy is maximum at the interface, and it rapidly decreases within 5 Å, but remarkably, across the arm length of a disclination dipole, the energy is not at the highest at the interface but a few Å apart, due to the additional contribution of the shear stresses to that of curvatures. The shear stress correspondingly reaches 8 GPa.

The tilt boundary energy is now plotted *vs.* the tilt angle in Fig. 9, and compared with predictions of other models, including a recent DSUM-based static model (Upadhyay et al., 2011) and atomistic simulations (Bachurin et al., 2003). When the initial disclination dipole distribution is based on the DSUM (configuration (a)), zero energy cusps are obtained for the 0°, 36.87°, 53.13° and 90° favored boundaries, and the largest energy values correspond to the highest misorientations relative to these boundaries. However, this energy level remains exceedingly small, as compared with atomistic predictions. In the Upadhyay et al. (2011) model, the strain and curvature contributions to the elastic energy are accounted for, but the energy level still remains underestimated in this range, due to discreteness of the disclination dipoles. When the actual structure of the boundary is accounted for by relaxing initial configuration (b), the boundary energies predicted by the present model reach the levels obtained from molecular statics calculations and display a similar distribution.

7. Conclusions

Capitalizing on the powerful tools of differential geometry and the theory of partial differential equations, the modeling paradigm in this study is to account for lattice incompatibility in a continuous fashion, focusing on the fields of density of lattice defects rather than on the atoms themselves. Thus, the elasto-plastic theory of crystal defect fields (Fressengeas et al., 2011) was used to model grain boundaries in a continuous manner. The theory accounts for the rotational and translational incompatibility of the lattice associated with the presence of disclinations and dislocations, and describes the latter by continuous densities. The material displacement, strain and curvature, are also defined continuously, even at a resolution length scale below interatomic distance. It is further assumed that, at this scale, the material is capable of transmitting stresses and couple-stresses. Dynamic tilt boundary modeling uses periodic arrangements of discrete wedge disclination dipoles as initial conditions. The latter relax by transport in their own couple-stress field into self-organized dislocation–disclination periodic patterns representing the atomistic structural units. The actual tilt angle values are retrieved by the model, if conveniently designed initial disclination walls are used, but the relaxation process is seen as crucial for the emergence of the correct grain boundary structure. The tilt angle is defined continuously across the boundary, though its variation essentially takes place within a thin, but non-singular, nanometric layer. Most of the elastic energy of the tilt boundary is also localized in this layer. The energy arises from a tension/compression state in disclination-rich areas, in good agreement with atomistic observations, and from curvature and shear in areas located within and between the disclination dipoles.

It is to be noted that the model remains oversimplified on several accounts. First, a small perturbation approach is used, which may become questionable in the small tension/compression patches dotted along the interface, where the trace of

the elastic strain tensor can reach values as high as 25%. Second, linear elasticity is employed and the dependence of the elastic constants on pressure is ignored, which may become inappropriate in such circumstances. Further, the elastic constants for the couple-stresses in copper are yet unknown, and were only roughly estimated in the present work. Despite these shortcomings, the tilt boundary energy *vs.* tilt angle predictions in Fig. 9 compares strikingly well with molecular statics predictions for copper, without making use of any *ad hoc* fitting parameter. In addition to a detailed rendering of the boundary structure, we consider this excellent agreement as a strong argument in favor of the present field approach of grain boundaries. From the point of view of differential geometry, field modeling is fully appropriate at length scales below the elementary lattice parameters, and it is rather meaningful that the predictions on GB energy of a field theory of crystal defects show good agreement with results from atomistic modeling (Bachurin et al., 2003). A more complete comparison with atomistic simulations involving field information and boundary structure will be provided in a forthcoming paper.

Finally, because it avoids resolving in time the atomic vibrations, the present approach allows using much larger time steps and smaller loading rates than molecular dynamics methods. Therefore, we believe that the present approach has an interesting potential for further modeling of grain boundaries and grain-boundary mediated plasticity.

Acknowledgments

The authors benefited of financial support from the ANR (Agence Nationale de la Recherche) under grant ANR-11-JS09-007-01, NanoMec.

References

Acharya, A., 2001. A model of crystal plasticity based on the theory of continuously distributed dislocations. J. Mech. Phys. Solids 49, 761.
Acharya, A., Fressengeas, C., 2012. Coupled phase transformation and plasticity as a field theory of deformation incompatibility. Int. J. Fract. 174, 87.
Bachurin, D.V., Murzaev, R.T., Nazarov, A.A., 2003. Atomistic computer and disclination simulation of [001] tilt boundaries in nickel and copper. Phys. Met. Metallogr. 96, 555.
Beausir, B., Fressengeas, C. Disclination densities from EBSD orientation mapping. Int. J. Solids. Struct., 10.1016/j.ijsolstr.2012.09.016, in press.
Bilby, B.A., 1955. Types of dislocation source. In: Bristol Conference Report on Defects in Crystalline Solids. The Physical Society, London, p. 124.
Cahn, J.W., Mishin, Y., Suzuki, A., 2006. Coupling grain boundary motion to shear deformation. Acta Mater. 54, 4953–4975.
deWit, R., 1970. Linear theory of static disclinations. In: Simmons, J.A., deWit, R., Bullough, R. (Eds.), Fundamental Aspects of Dislocation Theory. NBS Special Publication.
deWit, R., 1973. Theory of disclinations: IV. Straight disclinations. J. Res. Natl. Bur. Stand. A: Phys. Chem. 77A, 607–658.
Frank, F.C., 1950. The resultant content of dislocations in an arbitrary intercrystalline boundary. In: Symposium on the Plastic Deformation of Crystalline Solids (NAVEXOS-P-834). Mellon Institute, Pittsburgh, p. 150.
Fressengeas, C., Taupin, V., Capolungo, L., 2011. An elasto-plastic theory of dislocation and disclination fields. Int. J. Solids Struct. 48, 3499–3509.
Fressengeas, C., Taupin, V., Capolungo, L., Upadhyay, M., 2012. Tangential continuity of elastic/plastic curvature and strain at interfaces. Int. J. Solids Struct. 49, 2660–2667.
Gertsman, Y.Yu., Nazarov, A.A., Romanov, A.E., Valiev, R.Z., Vladimirov, V.I., 1989. Disclination-structural unit model of grain boundaries. Philos. Mag. A 59, 1113.
Gurtin, M.E., Anand, L., 2008. Nanocrystalline grain boundaries that slip and separate: a gradient theory that accounts for grain-boundary stress and conditions at a triple junction. J. Mech. Phys. Solids 56, 184.
Hadjesfandiari, A.R., Dargush, G.F., 2011. Couple stress theory for solids. Int. J. Solids Struct. 48, 2496–2510.
Huang, W., Mura, T., 1970. Elastic fields and energies of a circular edge disclination and a straight screw disclination. J. Appl. Phys. 41, 5175.
Kleman, M., Friedel, J., 2008. Disclinations, dislocations, and continuous defects: a reappraisal. Rev. Mod. Phys. 80, 61.
Kröner, E., 1963. On the physical reality of torque stresses in continuum mechanics. Int. J. Eng. Sci. 1, 261–278.
Li, J.C.M., 1972. Disclination model of high angle grain boundaries. Surf. Sci. 31, 12.
Mindlin, R.D., Tiersten, H.F., 1962. Effects of couple-stresses in linear elasticity. Arch. Ration. Mech. Anal. 11, 415.
Romanov, A.E., Kolesnikova, A.L., 2009. Application of disclination concept to solid structures. Prog. Mater. Sci. 54, 740.
Romanov, A.E., Vladimirov, V.I., 1992. Disclinations in crystalline solids. In: Nabarro, F.R.N. (Ed.), Dislocations in Solids, vol. 9. . Elsevier, Amsterdam, pp. 191.
Shih, K.K., Li, J.C.M., 1975. Energy of grain boundaries between cusp misorientations. Surf. Sci. 50, 109.
Shu, J.Y., King, W.E., Fleck, N.A., 1999. Finite elements for materials with strain gradient effects. Int. J. Numer. Methods Eng. 44, 373.
Spearot, D., 2005. Atomistic Calculations of Nanoscale Interface Behavior in FCC Metals. PhD Thesis. Georgia Institute of Technology.
Sutton, A.P., Vitek, V., 1983. On the structure of tilt grain boundaries in cubic metals. I. Symmetrical tilt boundaries. Philos. Trans. R. Soc. Lond. A 309, 1.
Upadhyay, M., Capolungo, L., Taupin, V., Fressengeas, C., 2011. Grain boundary and triple junction energies in crystalline media: a disclination based approach. Int. J. Solids Struct. 48, 3176–3193.
Upadhyay, M., Capolungo, L., Taupin, V., Fressengeas, C. Elastic constitutive laws in incompatible media, Phil. Mag., accepted.
Varadhan, S., Beaudoin, A.J., Acharya, A., Fressengeas, C., 2006. Dislocation transport using an explicit Galerkin/Least-Squares formulation. Model. Simul. Mater. Sci. Eng. 14, 1.
Warner, D.H., Sansoz, F., Molinari, J.F., 2006. Atomistic based continuum investigation of plastic deformation in nanocrystalline copper. Int. J. Plast. 22, 754–774.
Wei, Y.J., Anand, L., 2004. Grain-boundary sliding and separation in polycrystalline metals: application to nanocrystalline fcc metals. J. Mech. Phys. Solids 52, 2587.
Wei, Y., Gao, H., Bower, A.F., 2009. Numerical simulations of crack deflection at a twist-misoriented grain boundary between two ideally brittle crystals. J. Mech. Phys. Solids 57, 1865.
Zbib, H.M., Overman, C.T., Akasheh, F., Bahr, D., 2011. Analysis of plastic deformation in nanoscale metallic multilayers with coherent and incoherent interfaces. Int. J. Plast. 27, 1618–1639.